Photon density waves scattered from cylindrical inhomogeneities: theory and experiments

Scott A. Walker, David A. Boas, and Enrico Gratton

We present an analytical solution for the scattering of diffuse photon density waves from an infinite circular, cylindrical inhomogeneity embedded in a homogeneous highly scattering turbid medium. The analytical solution, based on the diffusion approximation of the Boltzmann transport equation, represents the contribution of the cylindrical inhomogeneity as a series of modified Bessel functions integrated from zero to infinity and weighted by different angular dependencies. This series is truncated at the desired precision, similar to the Mie theory. We introduce new boundary conditions that account for specular reflections at the interface between the background medium and the cylindrical inhomogeneity. These new boundary conditions allow the separate recovery of the index of refraction of an object from its absorption and reduced scattering coefficients. The analytical solution is compared with data obtained experimentally to evaluate the predictive capability of the model. Optical properties of known cylindrical objects are recovered accurately. However, as the radius of the cylinder decreases, the required measurement signal-to-noise ratio rapidly increases. Because of the new boundary conditions, an upper limit can be placed on the recovered size of cylindrical objects with radii below 0.3 cm if they have a substantially different index of refraction from that of the background medium.

OCIS codes: 120.5710, 160.4760, 170.5280.

1. Introduction

Useful information about turbid media such as human tissue can be derived from diffusing near-infrared photons in the medium. It has been shown that diffusing photons can give information about the average absorption and the scattering properties[1] of the medium as well as detection and characterization of inhomogeneities.[2,3] These results, coupled with tomographic algorithms, have application to tissue functional imaging as well as to the location of hematomas and tumors in the human body.[4,5] Historically, several groups have derived analytic solutions in both time and frequency domains describing a variety of shapes of inhomogeneities in different sampling geometries.[3,6,7] Solutions have been verified experimentally with frequency-domain data both for an infinitely absorbing edge[7] and for a sphere[3] embedded in an infinite macroscopically homogeneous turbid medium. These solutions are derived by employing boundary conditions that require continuity of the photon fluence and the normal component of the photon flux at the surface of the inhomogeneity. We present an analytical solution for the scattering of diffuse photon density waves (DPDW's) from an infinite cylindrical object embedded in an infinite turbid medium, employ modified boundary conditions that take into account the index of refraction mismatch between the embedded object and the turbid medium. We compare our solution with frequency-domain data and recover optical properties of embedded objects.

The random walk of photons in a highly scattering medium can be modeled by the Boltzmann transport equation. DPDW's arise out of the solution of the diffusion approximation of the Boltzmann transport equation for a sinusoidally intensity-modulated light source. This approximation depends on isotropic scattering of photons in the sampled medium and is valid far from boundaries.[8] DPDW's are spherical waves that are exponentially attenuated, depending on the absorption and the scattering properties of the highly scattering medium. Heterogeneities in the medium will cause the wave front to be deformed,

S. A. Walker and E. Gratton are with the Laboratory for Fluorescence Dynamics, Department of Physics, University of Illinois at Urbana-Champaign, 1110 West Green Street, Urbana, Illinois 61801-3080. D. A. Boas is with the Electro Optics Center, Tufts University, 4 Colby Street, Medford, Maryland 02155.

Received 23 June 1997; revised manuscript received 13 November 1997.

0003-6935/98/101935-10$15.00/0

allowing for the detection and possibly the characterization of a given object if the perturbing effect of the object on the amplitude and the phase of the wave is larger than the background noise level.

Since the Helmholtz equation is known to describe the transport of DPDW's in a piecewise homogeneous scattering medium,[7] we can derive an exact solution for the scattering of DPDW's by cylinders, which is similar to the solution for scattering from spheres derived by Boas *et al.*[9] The system we investigated consists of an infinitely long cylinder of highly scattering material embedded in another medium that is highly scattering and is infinite in extent.

To evaluate the validity of the diffusion approximation and the predictive power of the model, we compared the analytic solution with experimental data taken on 10-cm-long cylinders of different radii and optical properties. When the analytical solution is used, both the size and the optical properties of the cylinders can be reconstructed by a simple inverse algorithm employing a chi-squared, minimization fitting procedure. We can independently recover the index of refraction difference between the object and the surrounding tissue for each object. We show that accuracy of optical characterization depends on the size and the index of refraction of each inhomogeneity. Given the signal-to-noise ratio for our data, we can optically characterize cylinders having radii as small as 0.5 cm. Through simulations we can also show characterization limits for a range of cylinder sizes and experimental signal-to-noise ratios.

To fit our experimental data, we must account for an index of refraction mismatch between the background medium ($n = 1.33$) and the infinite cylinder ($n = 1.8$) by using modified boundary conditions. These boundary conditions, previously used by other researches,[10,11] take into account light that undergoes Fresnel reflections at the cylinder surface. Note that the typical range for biological indexes of refraction is $1.3 < n < 1.5$ and the corrections to the amplitude and the phase of DPDW's in tumors due to index of refraction mismatches may be small.[12,13] Having verified the analytical solution experimentally, we calculate the effects of Fresnel reflections for cylinders with a smaller index of refraction (1.45) and a variety of optical properties. Also, note that as the radius of the cylindrical inhomogeneity decreases, its surface-to-volume ratio increases. Thus the importance of this surface-dependent effect increases for smaller sized objects. For the same reason, Fresnel effects are more important for spherical inhomogeneities than for infinitely long cylindrical inhomogeneities.

Finally, we have simulated and fit experimental data to determine signal-to-noise ratio requirements for the recovery of size and optical properties of cylindrical inhomogenieties in the presence (absence) of an index of refraction mismatch with the background medium. We have found that, given a reasonable signal-to-noise ratio, we can place an upper limit on the recovered size of cylinders with radii below 0.3 cm if the surface effect due to an index mismatch is present.

2. Theory

The propagation of photons in a scattering medium can be described by the Boltzmann transport equation. In highly scattering media, such as human tissues, the analytic expression for photon propagation can be simplified by a diffusion approximation to the Boltzmann transport equation. The limit of validity for this approximation has been discussed[11] and will not be repeated here. The resulting time-dependent diffusion equation can be written

$$\nabla^2\Phi(\mathbf{r}, t) - \frac{\mu_a}{D}\Phi(\mathbf{r}, t) - \frac{1}{vD}\frac{\partial\Phi(\mathbf{r}, t)}{\partial t} = -\frac{1}{D}S(\mathbf{r}, t), \tag{1}$$

where $\Phi(\mathbf{r}, t)$ is the photon fluence rate, v is the speed of light in the medium, $D = (3\mu_s')^{-1}$, μ_s' is the reduced scattering coefficient, μ_a is the absorption coefficient, and $S(\mathbf{r}, t)$ is the source term. For a sinusoidally intensity-modulated point source, one can factor out the time dependence from the time-dependent diffusion equation by assuming a solution of the form

$$\Phi(\mathbf{r}, t) = \Phi_{dc}(\mathbf{r}, t) + \Phi_{ac}(\mathbf{r}, t)\exp(-i\omega t), \tag{2}$$

Thus Eq. (1) reduces to

$$(\nabla^2 + k^2)\Phi_{ac}(\mathbf{r}) = \frac{-q(\mathbf{r}, \omega)}{D}, \tag{3}$$

$$k^2 = \frac{-v\mu_a + i\omega}{vD}, \tag{4}$$

where ω is the frequency of source modulation, and $q(\mathbf{r}, \omega)$ is the source power per unit volume. Given the nature of the boundary conditions we must satisfy, it is easiest to expand the solution to the Helmholtz equation in a cylindrical geometry (Fig. 1). Here we assume that $\phi_s = 0$ and $z_s = 0$, and we place the source on the x axis. The general form for the solution to the Helmholtz equation for a sinusoidally oscillating point source at position $\mathbf{r}_s$ is

$$\Phi_{inc}(\mathbf{r}_s, \mathbf{r}_d) = S\frac{\exp(ik_{out}|\mathbf{r}_s - \mathbf{r}_d|)}{4\pi D|\mathbf{r}_s - \mathbf{r}_d|}, \tag{5}$$

where k_{out} is the DPDW wave number outside the cylinder, $\mathbf{r}_d$ is the position of the detector, and S is the source power. We place the source outside the cylinder on the x axis by assuming that $\rho_s = |\mathbf{r}_s| > a$ and expand the result in cylindrical coordinates[14]:

$$\Phi_{inc}(\mathbf{r}_s, \mathbf{r}_d) = \frac{S}{2\pi^2 D_{out}}\sum_{n=0}^{\infty}\int_0^{\infty} dp\, \cos(n\phi_d) \times \cos(pz_d)I_n(x_<)K_n(x_>). \tag{6}$$

Here D_{out} represents the diffusion coefficient outside the cylinder, I_n and K_n are the modified Bessel functions where $x_< = (p^2 - k_{out}^2)^{1/2}\rho_<$ and $x_> = (p^2 - k_{out}^2)^{1/2}\rho>$ and $\rho_<(\rho_>)$ is the smaller (larger) of ρ_s and ρ_d. The summation over n and the integral over p arise from the separation of variables in the Helm-

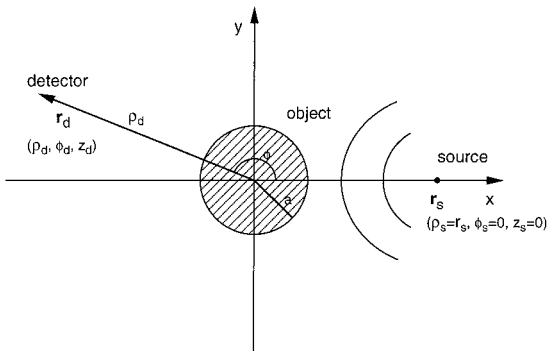

Fig. 1. Helmholtz equation solved in cylindrical coordinates with the origin at the object center. The source is positioned on the x axis ($\phi_s = 0$, $\rho_s = r_s$, and $z_s = 0$), and the axis of the infinite cylinder is along the z axis (coming out of the page). Sample contours of equal phase of the incoming spherical wave are shown before interaction with the cylinder. The radius of the cylinder is a and the vector pointing to the detector is $\mathbf{r}_d$ (ϕ_d, ρ_d, and z_d).

holtz equation after transformation into cylindrical coordinates. This solution represents an outgoing spherical wave. When this spherical wave is incident upon an infinitely long cylindrical inhomogeneity, the wave front is distorted. One can calculate this distortion by applying appropriate boundary conditions at the cylinder surface and solving for the photon density outside the cylinder. Outside the cylinder, the photon density is a superposition of the incident and the scattered waves, i.e., $\Phi_{\text{out}} = \Phi_{\text{inc}} + \Phi_{\text{scatt.}}$ Φ_{inc} is shown in Eq. (6) and

$$\Phi_{\text{scatt}}(\mathbf{r}_s, \mathbf{r}_d) = \sum_{n=0}^{\infty} \int_0^{\infty} dp \cos(n\phi_d)\cos(pz_d) \times [A_n(p)I_n(x) + B_n(p)K_n(x)]. \quad (7)$$

The most general solution for the wave inside the cylinder is

$$\Phi_{\text{in}}(\mathbf{r}_s, \mathbf{r}_d) = \sum_{n=0}^{\infty} \int_0^{\infty} dp \cos(n\phi_d)\cos(pz_d) \times [C_n(p)I_n(y) + D_n(p)K_n(y)], \quad (8)$$

where $x = (p^2 - k_{\text{out}}{}^2)^{1/2}\rho_d$ and $y = (p^2 - k_{\text{in}}{}^2)^{1/2}\rho_d$. Here k_{in} (k_{out}) is the DPDW wave number inside (outside) the cylinder. One determines the unknown parameters $A_n(p)$, $B_n(p)$, $C_n(p)$, and $D_n(p)$ by applying the following boundary conditions[9,11]:

(1) $\Phi_{\text{scatt}} -> 0$ as $\rho -> 0$.

(2) Φ_{in} is finite everywhere.

(3) $$(1 - R_{21})\Phi_{\text{out}} = \left[(1 - R_{21}) + 2(R_{12} - R_{21})D_{\text{in}}\frac{\partial}{\partial\rho}\right]\Phi_{\text{in}} \text{ at } \rho = a. \quad (9)$$

(4) $$D_{\text{out}}\frac{\partial}{\partial\rho}\Phi_{\text{out}} = D_{\text{in}}\frac{\partial}{\partial\rho}\Phi_{\text{in}} \text{ at } \rho = a. \quad (10)$$

Boundary condition 3 shows a discontinuity in the fluence inside and outside the object, which depends on the effective reflection coefficients R_{12} and R_{21}.[11] This is because not all the light incident on the cylindrical boundary is transmitted into (or out of) the cylinder. Here

$$R_{12} \equiv \frac{R_{12}{}^{\phi} + R_{12}{}^{j}}{2 - R_{12}{}^{\phi} + R_{12}{}^{j}}, \quad (11)$$

$$R_{12}{}^{\phi} \equiv \int_0^{\pi/2} 2\sin(\theta)\cos(\theta)R_{\text{fr}}{}^{12}(\theta)d\theta, \quad (12)$$

$$R_{12}{}^{j} \equiv \int_0^{\pi/2} 3\sin(\theta)\cos^2(\theta)R_{\text{fr}}{}^{12}(\theta)d\theta, \quad (13)$$

where the Fresnel reflection coefficient R_{fr} is defined as

$$R_{\text{fr}}(\theta) = \frac{1}{2}\left(\frac{n\cos(\theta') - n_{\text{out}}\cos(\theta)}{n\cos(\theta') + n_{\text{out}}\cos(\theta)}\right)^2 + \frac{1}{2}\left(\frac{n\cos(\theta) - n_{\text{out}}\cos(\theta')}{n\cos(\theta) + n_{\text{out}}\cos(\theta')}\right)^2 \quad \text{when} \quad 0 \le \theta \le \theta_c$$
$$= 1 \quad \text{when} \quad \theta_c \le \theta \le \pi/2 \quad (14)$$

$$n\sin(\theta) = n_{\text{out}}\sin(\theta'). \quad (15)$$

Considering these boundary conditions, we find that for Φ_{out}

$$A_n(p) = D_n(p) = 0, \quad (16)$$

$$B_n(p) = -\frac{S}{2\pi^2 D_{\text{out}}}K_n(z_b) \times \frac{D_{\text{out}}x_b I_n'(x_b)I_n(y_b)X_{\text{fr}} - D_{\text{in}}y_b I_n(x_b)I_n'(y_b)}{D_{\text{out}}x_b K_n'(x_b)I_n(y_b)X_{\text{fr}} - D_{\text{in}}y_b K_n(x_b)I_n'(y_b)}, \quad (17)$$

and

$$C_n(p) = -\frac{S}{2\pi^2 D_{\text{out}}}K_n(z_b) \times \frac{D_{\text{out}}x_b K_n(x_b)I_n'(x_b) - D_{\text{out}}x_b K_n'(x_b)I_n(x_b)}{D_{\text{out}}x_b K_n'(x_b)I_n(y_b)X_{\text{fr}} - D_{\text{in}}y_b K_n(x_b)I_n'(y_b)}, \quad (18)$$

$$X_{\text{fr}} = \left[\frac{(1 - R_{12})}{(1 - R_{21})} + \frac{2(R_{12} - R_{21})}{(1 - R_{21})}D_{\text{in}}\frac{y_b}{a}\frac{I_n'(y)}{I_n(y)}\right], \quad (19)$$

where $x_b = (p^2 - k_{\text{out}}{}^2)^{1/2}a$, $y_b = (p^2 - k_{\text{in}}{}^2)^{1/2}a$, $z_b = (p^2 - k_{\text{in}}{}^2)^{1/2}\rho_s$.

This solution accounts for the effects of the index of refraction mismatch between the cylinder and the background medium in two ways: First, the speed of light is changed in the inhomogeneity; second, Fresnel reflections cause a discontinuity in the flu-

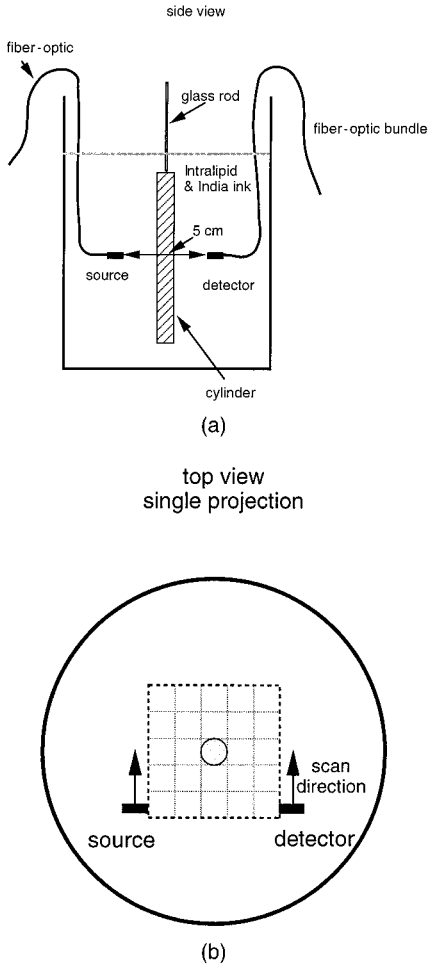

Fig. 2. Experimental setup. (a) Side view of the 16-L glass container filled with Intralipid/India Ink mixture. Fiber optics carry light to the source and from the detector. The fiber tips are separated by 5 cm inside the tank and scanned by means of a mechanical *XYZ* scanner with a positioning accuracy of 10 μm. The object is suspended in the medium by a 3-mm-diameter glass rod. (b) Top view of the cylinder. The source and the detector make a one-dimensional scan perpendicular to the object across the volume of interest. Each scan consists of 41 measurements at 2-mm intervals for a total of 8 cm.

ence across the boundary between the cylinder and the background medium.

3. Materials and Methods

The experimental setup for the measurement of the front of the DPDW has been previously presented[15] and is repeated briefly here. Measurements are conducted in a quasi-infinite geometry with a frequency-domain spectrometer and an *XYZ* positioning scanner. A 120-MHz radio-frequency signal is amplified and sent to a 50-mW laser diode ($\lambda = 793$ nm) coupled to a 1-mm fiber-optic conduit to channel the near-infrared light into the turbid medium. The coupling efficiency with the laser diode is 20%, giving an output power of approximately 10 mW. Detected light is collected by a 0.3-cm diameter fiber-optic bundle and processed with

Table 1. Cylinder and Background Measured Optical Properties

Parameters	μ_a (cm^{-1})	μ_s' (cm^{-1})	n
Measured values of material A+[a]	0.18 ± 0.015	5.9 ± 1.0	1.8 ± 0.1
Measured values of material A−[a]	0.06 ± 0.01	5.0 ± 1.0	1.8 ± 0.1
Measured values of background medium (Intralipid + India ink)	0.079 ± 0.005	8.0 ± 0.1	1.333

[a] A± indicates more (less) absorbing than the background.

frequency-domain methods to measure the dc intensity, ac amplitude, and phase of the photon density wave. Source and detector optical fibers are scanned in tandem, facing each other, with a separation of 5 cm as shown in Fig. 2. Each linear scan consists of 41 measurements of the photon density wave taken at 0.2-cm steps for a total of 8 cm. Each scan is reproducible with a position error of 10 μm due to the *XYZ* positioning scanner. Measurements take place inside a large glass container of Intralipid fat emulsion mixed with black India ink. The volume of the container is 16 L. The concentrations of Intralipid and India ink are adjusted to give optical coefficients $\mu_{a0} = 0.079\ cm^{-1}$ and $\mu_{s0}' = 7.9\ cm^{-1}$ as measured by the multidistance protocol.[16]

To model infinitely long cylinders, we cast 5 cylinders each 10 cm long with 3 different radii (0.25, 0.5, and 0.75 cm) and having two sets of optical coefficients ($\mu_{a1} = 0.045\ cm^{-1}$, $\mu_{s1}' = 7.5\ cm^{-1}$, $\mu_{a2} = 0.13\ cm^{-1}$, and $\mu_{s2}' = 8.0\ cm^{-1}$) (Table 1). Each cylinder was made from a large block of hot melt glue that was characterized with a semi-infinite medium multidistance protocol.[8] We manipulated the reduced scattering coefficient of the block of glue by mixing highly scattering glue with clear glue, whereas we adjusted the absorption coefficient by adding different amounts of India ink to the glue during the mixing procedure. Owing to the optical coefficients of the background medium, the probability of a photon traveling from the source to the detector, which is approximately the end of a cylinder, is negligible. Thus we treat each cylinder as being infinitely long.

An experiment was performed to measure the index of refraction of the glue. After forming the clear glue into a right-angle prism, we directed light from a He–Ne laser ($\lambda = 632.8$) into the prism and measured the critical angle for total internal reflection. From this measurement we employed Snell's law to extract the index of refraction of the glue.

Results are divided into analysis of experimental data and simulations. Experiments were performed to verify the validity of the theory and to investigate its predictive power for characterizing each cylindrical inhomogeneity in terms of radius, absorption, reduced scattering coefficient, and index of refraction. Each cylinder is located midway between the source and the detector (as in Fig. 2). The phase and the

Table 2. Cylinder and Background Recovered Optical Properties

Radius (cm)	μ_a (cm^{-1})	μ_s' (cm^{-1})	n	Reduced χ^2
		Type A+[a]		
0.75	0.183 ± 0.005	7.1 ± 0.1	1.7 ± 0.05	1.6
0.5	0.181 ± 0.007	6.4 ± 0.2	1.75 ± 0.08	1.0
0.25	0.171 ± 0.03	6.6 ± 1.2	1.65 ± 0.4	1.2
		Type A−[a]		
0.75	0.073 ± 0.001	4.5 ± 0.2	1.8 ± 0.05	1.2
0.5	0.081 ± 0.001	4.2 ± 0.4	1.8 ± 0.07	1.1

[a]A± indicates more (less) absorbing than the background.

amplitude of DPDW's are recorded as the source and the detector perform a linear scan across the object. We fit the resulting data set by implementing the analytical solution given in Eqs. (6)–(19) with a least-squares-fitting procedure inside the photon migration imaging (PMI) program developed at the University of Pennsylvania.

To obtain further analysis of the implications of the new boundary conditions introduced in Eq. (9), we performed two additional simulations. The first simulation determines the effect of a realistic index of refraction mismatch on a measured DPDW phase and an ac amplitude for a variety of object absorption and scattering parameters. The second simulation determines the required signal-to-noise ratio levels for the optical characterization of cylinders of various radii. Both simulations are performed with the PMI program.

4. Results

A. Analysis of Experimental Data

1. Fit of μ_a, μ_s', and n for a Given Cylinder Radius

To demonstrate the predictive ability of the analytic solution, we fit the data from the first experiment with Eqs. (1)–(19) to compare predicted optical properties of the cylindrical inhomogeneities with the measured optical properties for a range of cylinder radii. The position of each cylinder is considered to be known (this is a good assumption because the accuracy in locating the center of each cylinder is determined only by the accuracy of placement of the source and the detector), whereas the absorption and the reduced scattering parameters of the cylinder are treated as free parameters. Table 2 demonstrates the agreement between theory and experiment given an infinite cylinder of known radius. A sample fit of the analytical solution to the experimental data is shown in Fig. 3. Note that in the fit, the radius of the cylinder is fixed to the correct radius. Under this assumption, the scattering and the absorption coefficients as well as the index of refraction mismatch for a cylinder can be recovered independently.

2. Separation of Object Size and Absorption Coefficient for Cylinders of Various Radii

We also fit the experimental data, assuming a range of cylinder radii to determine whether each cylinder's size and optical properties can be separately determined. Figures 4(a)–4(c) show the result of fitting

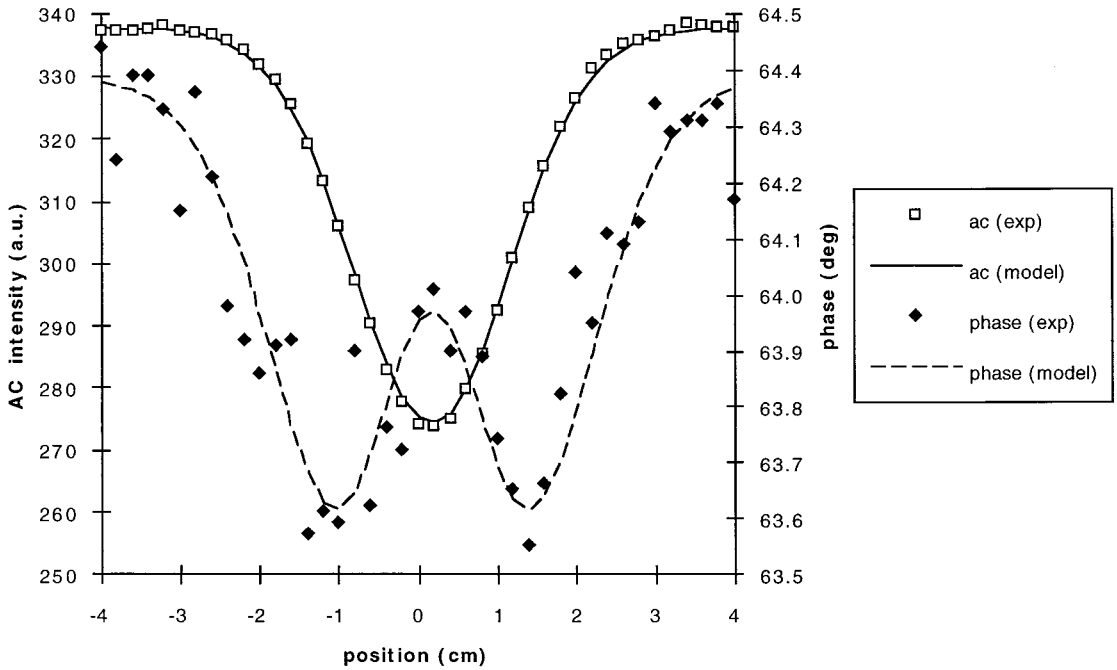

Fig. 3. Sample fits to experimental data are presented for a 0.5-cm-radius cylinder of material type A− (Table 1). The open squares and the filled diamonds represent the ac and the phase measurements, respectively. The theory is represented by the solid and the dotted curves for ac and phase predictions. The experimental parameters are given in Table 1.

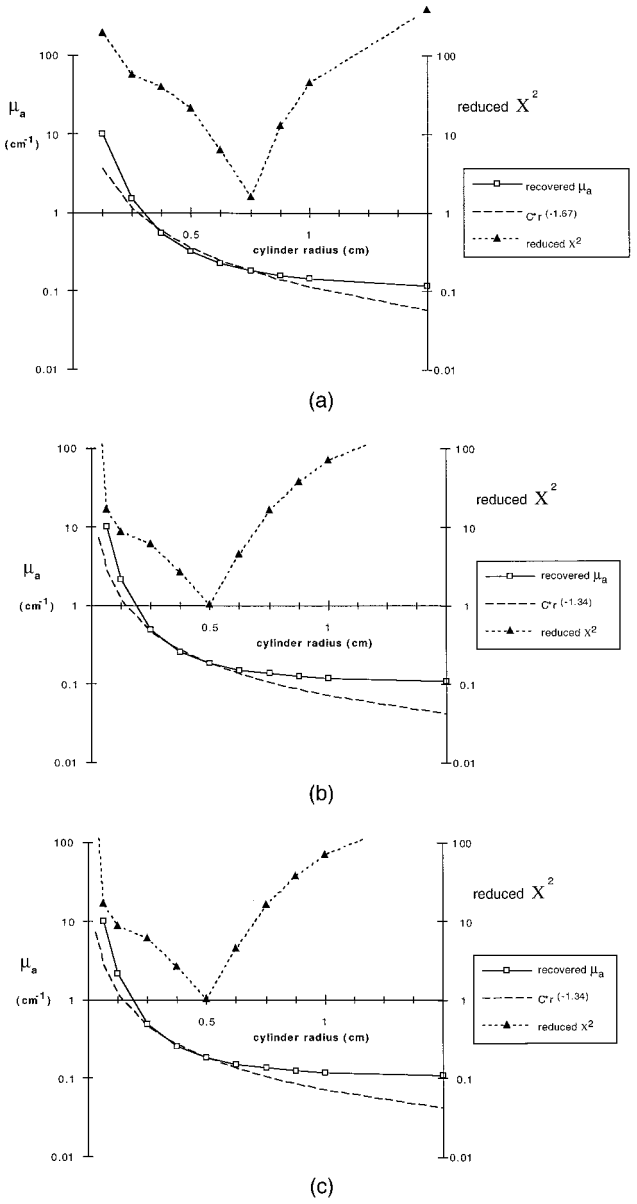

Fig. 4. Comparison of the precision of optical property recovery for different sized cylinders. As the radius of each cylinder decreases, the object's absorption coefficient cannot be determined independently from its radius. Open squares represent the best fit to experimental data by varying the absorption coefficient μ_a at different assumed cylinder radii. Filled triangles represent the goodness of fit as measured by the reduced χ^2 ($\Delta AC_{meas} = 0.2\%$, $\Delta Phase_{meas} = 0.1°$). (a) True cylinder radius, 0.75 cm. The dotted curve represents an approximation of the absorption versus the radius ($\propto r^{-1.67}$) normalized to the value of μ_a at the true radius ($r = 0.75 \pm 0.02$ cm). (b) True cylinder radius, 0.5 cm. The dotted curve represents an approximation of the absorption versus the radius ($\propto r^{-1.34}$) normalized to the value of μ_a at the true radius ($r = 0.5 \pm 0.1$ cm). (c) True cylinder radius, 0.25 cm. The dotted curve represents an approximation of the absorption versus the radius ($\propto r^{-0.97}$) normalized to the value of μ_a at the true radius. Owing to the small radius of this cylinder, the true radius cannot be determined independently from the absorption coefficient.

experimental data for three different sized cylinders for a range of assumed cylinder radii. For each fit, we assume the best-fit value for the reduced scattering and the index of refraction of the cylinder from Table 2. The cylinder radius ranges from 0.032 to 2 cm. To fit the model to experimental data, we allow the absorption coefficient inside the cylinder to vary. The resulting values of μ_a are represented by the open squares, whereas the filled triangles show the values of reduced χ^2 obtained for each fit. (Experimental measurement errors are $\Delta AC_{meas} = 0.2\%$?, $\Delta Phase_{meas} = 0.1°$.)

Figure 4(a) shows a minimum reduced χ^2 value of 1.58 at the true radius of 0.75 cm. If we determine a range of possible radii for this cylinder by assuming a confidence interval for μ_a of 67%, the recovered radius and the absorption coefficient are $r = 0.75 \pm 0.02$ cm and $\mu_a = 0.183 \pm 0.005$ cm^{-1}, respectively. The sharp decrease in the reduced χ^2 plot shows that the radius and the absorption coefficient are easily separated in this case. In Fig. 4(b), the true cylinder radius is 0.5 cm and the recovered radius and the absorption coefficient are $r = 0.5 \pm 0.04$ cm and $\mu_a = 0.18 \pm 0.04$ cm^{-1}, respectively. Still the size and the absorption coefficient are recovered separately. Finally, in Fig. 4(c), the true cylinder radius is 0.25 cm and the recovered radius and the absorption coefficient cannot be recovered independently. This result suggests that for smaller cylinders, the absorption coefficient for the cylinder cannot be recovered without *a priori* knowledge of the cylinder's size. However, the data show only that the radius of the object must be smaller than 0.4 cm.

Figures 4(a)–4(c) illustrate the idea that smaller inhomogeneities are more difficult to characterize because their optical properties and size cannot be separately determined. As the true radius of the cylinder decreases, uncertainty in the prediction of optical properties by the theoretical model arises from compensation between the size (radius of the cylinder) and the absorption optical properties of the cylinder. These experimental results match theoretical predictions made by other researchers for spherical objects.[9]

3. *Evaluation of Surface–Volume Effect*

For a cylinder with a fixed radius, we can determine the relative magnitudes of cylinder surface and volume effects on the perturbation of the DPDW by looking at the functional relationship between the best-fit absorption coefficient and the assumed object radius over a range of assumed radii [Figs. 4(a)–4(c)]. We expect a relationship of the form $\mu_a = C^* r^k$. From previous work with a spherical object,[9] we see that a volume perturbation results in a relationship of $\mu_a = C^* r^{-3}$. It is reasonable to assume that a surface perturbation would result in a relationship of the form $\mu_a = C^* r^{-2}$. Thus we see for a spherical object with a volume perturbation that μ_a varies inversely as the assumed volume. Given a surface perturbation, μ_a varies inversely with the assumed surface area. Applying this to a cylindrical object, we expect that a volume perturbation will result in $\mu_a = C^* r^{-2}$

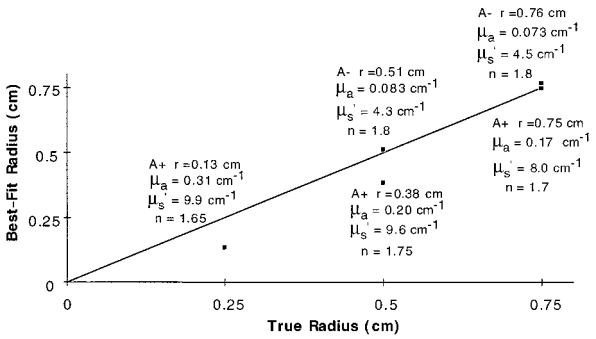

Fig. 5. Best fit of the analytical solution to measured data varying μ_a, μ_s', n, and radius. Filled squares represent the best-fit radius of each cylinder plotted versus the true radius. Recovered values of the cylinder optical properties can be compared with the values in Table 1. The values for the largest cylinders are recovered most accurately. As the cylinder radius decreases, the size and the optical properties of each cylinder are separated less accurately.

and that a surface perturbation will result in $\mu_a = C^* r^{-1}$.

The curves for three different cylinders are shown by the dotted curves in Figs. 4(a)–4(c). Here the best-fit value of k ranges from -1.67 for the 0.75-cm-diameter cylinder to -0.97 for the 0.25-cm-diameter cylinder. The value of $k = -0.97$ for the 0.25-cm-diameter cylinder suggests that the perturbations in the measured phase and the ac are proportional to the cylinder surface area rather than the cylinder volume. As the cylinder radius decreases from 0.75 to 0.25 cm, the surface-to-volume ratio for each cylinder increases. This suggests that effects due to Fresnel reflections at the surface of each cylinder become larger relative to the volume-dependent effects due to the absorption and the reduced scattering parameters of the cylinders.

4. *Fit of μ_a, μ_s', and Cylinder Radius*

Finally, results are shown for the best fit of the analytical solution to measured data varying μ_a, μ_s', n, and radius. Values of the best-fit radius are plotted versus the true radius in Fig. 5 for all samples shown in Table 2. Recovered values of the cylinder optical properties, shown on the graph for each point, can be compared with the values in Table 1. The values for the largest cylinders are recovered most accurately. As the cylinder radius decreases, the size and optical properties of each cylinder are recovered with less accuracy.

B. Simulations

1. *Evaluation of Object μ_a and μ_s' Effects*

For the experimental case considered here we see that Fresnel reflections are significant when the index mismatch is 1.33–1.8. However, for tissue in which the index mismatch is much less (i.e., $1.3 < n < 1.5$),[12,13] we expect the Fresnel reflections to be less significant. We have simulations to determine the effect of introducing Fresnel reflection boundary

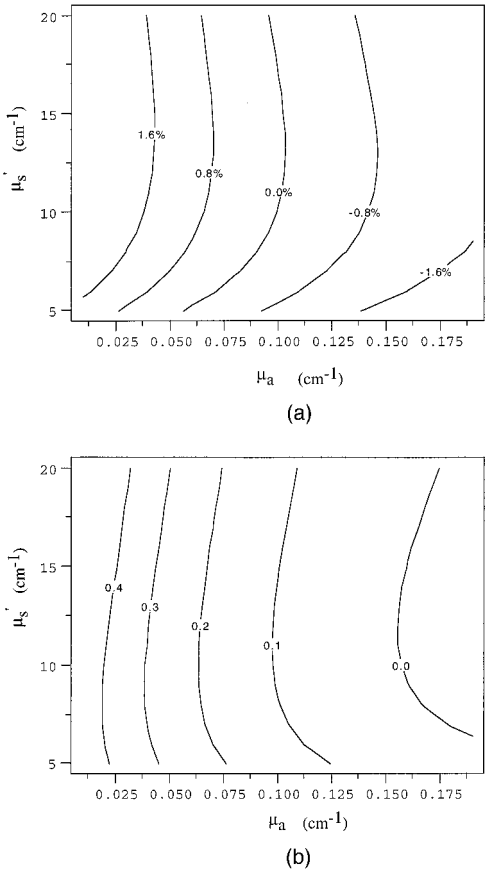

Fig. 6. Effect of Fresnel reflections on measured ac and phase. The index of refraction mismatch between background and cylinder media is $n_{\text{background}} = 1.33$ versus $n_{\text{object}} = 1.45$. The infinite cylinder is centered between the source and the detector, which are separated by 5.0 cm. The background medium absorption and the scattering coefficients are $\mu_a = 0.1$ cm^{-1} and $\mu_s' = 10$ cm^{-1}, whereas the absorption and the scattering coefficients of the cylinder vary ($0.01 \text{ cm}^{-1} < \mu_a < 0.2 \text{ cm}^{-1}$, $5 \text{ cm}^{-1} < \mu_s' < 20 \text{ cm}^{-1}$). (a) Perturbation in measured ac intensity due to Fresnel reflections. As the cylinder becomes more (less) transparent than the background medium, the measured ac intensity is increased (decreased) owing to Fresnel reflections. (b) Difference in measured phase caused by Fresnel boundary conditions. This phase lag increases as the absorption coefficient of the cylinder decreases, reaching a maximum value of 0.5° when $\mu_a = 0.01$ cm^{-1}.

conditions for an index mismatch of $n_{\text{background}} = 1.33$ versus $n_{\text{object}} = 1.45$. This index mismatch represents an extreme case. Normal tissue indexes of refraction vary from 1.37 (liver) to 1.45 (adipose tissue).[12] The simulations are made for an infinite, 0.5-cm-radius cylinder. The cylinder is centered between the source and the detector, which are separated by 5.0 cm. The background medium optical properties were $\mu_a = 0.1$ cm^{-1} and $\mu_s' = 10$ cm^{-1}, whereas the optical properties of the cylinder varied ($0.01 \text{ cm}^{-1} < \mu_a < 0.2 \text{ cm}^{-1}$ and $5 \text{ cm}^{-1} < \mu_s' < 20$ cm^{-1}). We calculated the values in Fig. 6 by first solving Eqs. (1)–(19) for the experimental case shown and then by subtracting a solution that assumes the same experimental parameters but does not include Fresnel reflections.

Figure 6(a) shows the perturbation in measured ac intensity due to only Fresnel reflections. Note that when the optical properties of the cylinder are equal to the background optical properties, the ac intensity is not significantly perturbed by Fresnel reflections. As the cylinder becomes more (less) transparent than the background medium, the measured ac intensity is increased (decreased). Figure 6(b) shows the difference in measured phase caused by Fresnel boundary conditions. The phase lag increases as the absorption coefficient of the cylinder decreases, reaching a maximum value of 0.5° when $\mu_a = 0.01$ cm^{-1}. Note that the differences in measured phase due to the slower speed of light inside the cylinder are not included here.

Simulations have also been performed for a sphere with a 0.5-cm radius, and these show similar results with an increase by a factor of 2 in the magnitude of the effects due to Fresnel reflections compared with the cylinder simulations. One can explain this increase by noting that a sphere of equal radius has more surface area in regions of high photon density (near the source–detector axis) compared with an infinite cylinder.

2. *Differences in Experimental Data Generated by Different Sized Cylinders*

First, simulated experimental data are generated for the source–detector geometry shown in Fig. 2 with a cylinder of radius r_{true} (background: $\mu_a = 0.1$ cm^{-1}, $\mu_s' = 10$ cm^{-1}, $n_{background} = 1.33$; object: $\mu_a = 0.2$ cm^{-1}, $\mu_s' = 10$ cm^{-1}, $n_{object} = 1.33$). These data are then fit with the theoretical model by our varying the absorption coefficient of a single cylinder in the same position with an assumed radius r_{fitted}. We then make a simple estimate of the differences between the theoretical model (assumed radius) and the simulated data (true radius) by calculating the reduced χ^2. We could improve this estimate by accounting for the systematic nature of the deviations in phase and ac caused by the change in cylinder radius. Figure 7(a) shows curves of reduced $\chi^2 = 0.3$, 3, and 30 for our experimental conditions. Here the size of cylinders with a radius larger than 0.4 cm can be determined with increasing accuracy as the radius r_{true} increases. Note that in Fig. 7(a), lower limits cannot be determined for the size of cylinders with a true radius of 0.4 cm. However, by placing an upper limit of 0.7 cm on the radii of these objects, we can still provide important clinical information. As the radius r_{true} increases, the accuracy of size determination increases for a given set of experimental errors.

If we now add an index of refraction mismatch between the cylinder and the background medium with the same optical properties as above (background: $\mu_a = 0.1$ cm^{-1}, $\mu_s' = 10$ cm^{-1}, $n_{background} = 1.33$; object: $\mu_a = 0.2$ cm^{-1}, $\mu_s' = 10$ cm^{-1}, $n_{object} = 1.45$), we obtain the plot shown in Fig. 7(b). The effect of the object's different index of refraction is a decrease in the required signal-to-noise ratio for accurate recovery of a cylinder's size and optical properties as the true radius of the cylinder decreases to smaller than 0.4 cm. Also, the index of refraction mismatch allows the placement of a limit on the recovered size and the optical properties of cylinders with radii below 0.3 cm. A possible explanation of these differences is that the index mismatch produces a surface-dependent effect. Cylinders with smaller radii have a larger surface-to-volume ratio and there-

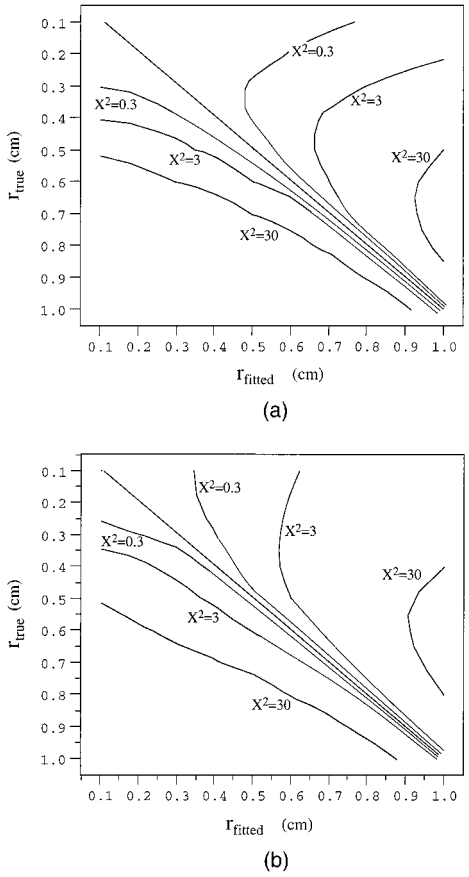

Fig. 7. Differences in experimental data generated by different-sized cylinders. Simulated experimental data are generated for the source–detector geometry shown in Fig. 2 with a cylinder of radius r_{true} (background: $\mu_a = 0.1$ cm^{-1}, $\mu_s' = 10$ cm^{-1}, $n_{background} = 1.33$; object: $\mu_a = 0.2$ cm^{-1}, $\mu_s' = 10$ cm^{-1}, $n_{object} = 1.33$). These data are then fit with the theoretical model by our varying the absorption coefficient of a single cylinder in the same position with an assumed radius r_{fitted}. We then make a simple evaluation of the differences between the theoretical model (assumed radius) and the simulated data (true radius) by calculating the reduced χ^2. (a) Lines of reduced $\chi^2 = 0.3$, 3, and 30 for our experimental conditions. Here the size of cylinders with a radius larger than 0.4 cm can be determined with increasing accuracy as the radius r_{true} increases. (b) Simulated data generated as in (a) by our adding an index of refraction mismatch between the background medium and the object ($n_{background} = 1.33$; $n_{object} = 1.45$). These data are then fitted as in (a). The effect of the object's different index of refraction is a decrease in the required signal-to-noise ratio for accurate recovery of a cylinder's size and optical properties as the true radius of the cylinder decreases to smaller than 0.4 cm. The index of refraction mismatch allows the placement of a limit on the recovered size and optical properties of cylinders with radii below 0.3 cm.

fore are characterized more by their surface properties.

5. Conclusion

We have presented an analytic solution for the scattering of DPDW's from cylindrical inhomogeneities embedded in a macroscopically homogeneous medium. The purpose of our study was to investigate in which conditions of cylinder radius and optical properties we can recover the size of an object and its optical parameters. The analytical solution allows us to reconstruct the object by fitting its geometrical and optical parameters. This ideal situation cannot be realized *in vivo*, but our purpose is to establish under the best possible situation what can be reconstructed. There is an underlying assumption in our approach, i.e., that the diffusion approximation to the Boltzmann transport equation is adequate to describe the scattering of DPDW in phantoms that simulate biological tissues. First, by plotting the solution on top of the data, we demonstrated that the analytical solution describes the data within the noise. A noticeable systematic deviation occurs if Fresnel reflections are not included. However, there is no apparent systematic deviation arising from the diffusion approximation *per se*. Second, using the analysis of the chi-squared surface, we used the analytical solution to evaluate the uncertainty of the recovered parameters. If we assume that the reduced chi square can fluctuate, giving a confidence interval of 67%, we can establish a range of values for the recovered parameters. Note that this procedure is not based on the analysis of the covariance matrix of error (that only accounts for first-order correlation), but our error analysis accounts for all orders of correlation between the parameters of the model.[17]

We have found that to fit our experimental data correctly and to avoid systematic deviations in the fits, we must include Fresnel reflection boundary conditions as implemented by Haskell *et al*.[11] These new boundary conditions allow us to recover the index of refraction of an object separately from its absorption and scattering coefficients. The magnitude of the effect due to Fresnel reflections from a cylindrical object embedded in a turbid medium depends on the index of refraction mismatch between the object and the background medium, the surface-to-volume ratio of the object, and the absorption and the scattering coefficients of the object. This effect should be more important for objects that are less absorbing than the background medium and for objects that have larger surface-to-volume ratio.

After including Fresnel reflection boundary conditions in the analytic solution, we showed by our experimental data that the optical properties of cylindrical objects can be recovered with fairly good accuracy for cylinders with radii greater than 0.25 cm. Since our solution is based on the diffusion approximation to the Boltzmann transport equation, these results also show the validity of the diffusion approximation in characterizing inhomogeneities with typical values of absorption and reduced scattering coefficients in a turbid medium. Given the typical noise of our measurements, we also show that the major source of uncertainty in predicting optical properties of a cylindrical inhomogeneity arises from compensation between the optical absorption coefficient and the size of the object, owing to the correlation between the absorption and the radius of the cylinder. The size of any cylinder can be differentiated from its absorption properties given a large enough signal-to-noise ratio; however, below this limit one can measure only an absorption density typical of a monopole perturbation. In our experimental conditions, this limit occurs between a radius of $r = 0.25$ and $r = 0.5$ cm. Through simulations, we have determined that an index of refraction mismatch between the cylinder and the background decreases signal-to-noise ratio requirements and makes possible the recovery of a limit on the size and the optical properties for cylinders with radii below 0.3 cm. Given these limits, shot-noise and positional errors for *in vivo* experiments will determine the range of sizes and the optical properties that can be differentiated.

Other factors that might improve the prospects for optical parameter recovery include the addition of finite medium boundary conditions, which are not considered in this paper. Also, the inclusion of other experimental variables, such as measurements at multiple modulation frequencies, might improve the accuracy of the recovered geometrical and optical parameters. Similarly, scanning multiple sources and detectors (instead of a single source–detector pair) can reduce the integration time to achieve a given signal-to-noise ratio as well as provide the ability to better characterize background optical properties.

The Laboratory for Fluorescence Dynamics is supported by the National Institutes of Health (NIH), grant RR03155, and by the University of Illinois at Urbana-Champaign. This research is also supported by NIH grant CA57032.

References

1. M. S. Patterson, B. Chance, and B. C. Wilson, "Time resolved reflectance and transmittance for the non-invasive measurement of optical properties," Appl. Opt. **28,** 2331–2336 (1989).
2. J. S. Maier and E. Gratton, "Frequency-domain methods in optical tomography: detection of localized absorbers and a backscattering reconstruction scheme," in *Photon Migration and Imaging in Random Media and Tissues*, B. Chance and R. R. Alfano, eds., Proc. SPIE **1888,** 440–451 (1993).
3. D. A. Boas, M. A. Oleary, B. Chance, and A. G. Yodh, "Scattering of diffuse photon density waves by spherical inhomogeneities within turbid media: analytic solution and applications," Proc. Natl. Acad. Sci. USA **91,** 4887–4891 (1994).
4. G. Gratton, M. Fabiani, D. Friedman, M. A. Franceschini, S. Fantini, P. M. Corballis, and E. Gratton, "Rapid changes of optical parameters in the human brain during a tapping task," J. Cognitive Neurosci. **7,** 446–456 (1994).
5. D. A. Benaron and D. K. Stevenson, "Optical time-of-flight and absorbance imaging of biologic media," Science **259,** 1463–1466 (1993).
6. S. R. Arridge, M. Cope, and D. T. Delpy, "The theoretical basis

for the determination of optical pathlengths in tissue: temporal and frequency analysis," Phys. Med. Biol. **37,** 1531–1560 (1992).
7. J. B. Fishkin and E. Gratton, "Propagation of photon-density waves in strongly scattering media containing an absorbing semi-infinite plane bounded by a straight edge," J. Opt. Soc. Am. A **10,** 127–140 (1993).
8. S. Fantini, M. A. Franceschini, and E. Gratton, "Semi-infinite-geometry boundary problem for light migration in highly scattering media: a frequency-domain study in the diffusion approximation," J. Opt. Soc. Am. B **11,** 2128–2138 (1994).
9. D. A. Boas, M. A. Oleary, B. Chance, and A. G. Yodh, "Detection and characterization of optical inhomogeneities with diffuse photon density waves: a signal-to-noise analysis," Appl. Opt. **36,** 75–92 (1997).
10. R. Aronson, "Boundary conditions for diffusion of light," J. Opt. Soc. Am. A **12,** 2532–2539 (1995).
11. R. C. Haskell, L. O. Svaasand, T.-T. Tsay, and B. J. Tromberg, "Boundary conditions for the diffusion equation in radiative transfer," J. Opt. Soc. Am. A **11,** 2727–2741 (1994).
12. F. P. Bolin, L. E. Preuss, R. C. Taylor, and R. J. Ference, "Refractive index of some mammalian tissues using a fiber optic cladding method," Appl. Opt. **28,** 2297–2302 (1989).
13. S. L. Jacques, C. A. Alter, and S. A. Prahl, "Angular dependence of HeNe laser light scattering by human dermis," Lasers Life Sci. **1,** 309–333 (1987).
14. J. D. Jackson, *Classical Electrodynamics* (Wiley, New York), Chap. 16.
15. S. A. Walker, S. Fantini, and E. Gratton, "Image reconstruction using back-projection from frequency domain optical measurements in highly scattering media," Appl. Opt. **35,** 170–179 (1996).
16. S. Fantini, M. A. Franceschini, J. B. Fishkin, B. Barbieri, and E. Gratton, "Quantitative determination of the absorption spectra of chromophores in strongly scattering media: a light-emitting-diode based technique," Appl. Opt. **33,** 5204–5213 (1994).
17. J. M. Beechem, E. Gratton, M. Ameloot, J. R. Knutson, and L. Brand, "The global analysis of fluorescence intensity and anisotropy decay data: second generation theory and programs," in *Topics in Fluorescence Spectroscopy*, *II*, J. R. Lakowicz, ed. (Plenum, New York, 1991), Chap. 5, pp. 241–305.